ceramics

Article

Erbium Orthoniobate-Tantalates: Structural, Luminescent and Mechanical Properties of $ErNb_xTa_{1-x}O_4$ Ceramics and Bactericidal Properties of $ErNbO_4$ Powder

Mikhail Palatnikov [1], Olga Shcherbina [1], Nadezhda Fokina [2], Maxim Smirnov [1], Elena Zelenina [3], Sofja Masloboeva [1] and Diana Manukovskaya [1,*]

[1] Tananaev Institute of Chemistry—Subdivision of the Federal Research Centre «Kola Science Centre of the Russian Academy of Sciences», 184209 Apatity, Russia; m.palatnikov@ksc.ru (M.P.); o.shcherbina@ksc.ru (O.S.); m.smirnov@ksc.ru (M.S.); sofia_masloboeva@mail.ru (S.M.)
[2] Institute of North Industrial Ecology Problems—Subdivision of the Federal Research Center «Kola Science Center of the Russian Academy of Sciences», 184209 Apatity, Russia; nadezdavf@yandex.ru
[3] Saint Petersburg State Institute of Technology, Moskovsky Prospect, Building 24-26/49 Litera A, 190013 Saint Petersburg, Russia; elena.v.zelenina@gmail.com
* Correspondence: d.manukovskaia@ksc.ru

Abstract

Fine powders of erbium niobate-tantalates $ErNb_xTa_{1-x}O_4$ (x = 0; 0.1; 0.3; 0.5; 0.7; 0.9; 1) have been synthesized by the liquid-phase method in this study. Ceramic samples have been prepared using conventional sintering from these powders. Rietveld refinement of XRD patterns of polycrystals determined the phase composition and clarified the parameters of the phase structure of $ErNb_xTa_{1-x}O_4$ solid solutions depending on the Nb/Ta ratio. The morphological features of the microstructure of erbium niobate-tantalate ceramics have been studied. Their mechanical properties, strength characteristics (Young's modulus, microhardness) and critical stress intensity factor of the first kind K_{IC} have been estimated. The photoluminescent properties of ceramic solid solutions of erbium niobate-tantalates depending on the composition have been studied. Dark and photoinduced toxicity of finely dispersed $ErNbO_4$ powders have been studied in relation to Gram-positive, Gram-negative and spore-forming microorganisms. The best indicators of antibacterial activity of $ErNbO_4$ have been demonstrated in relation to Gram-positive cells of *Micrococcus sp.* The discovered properties open up the possibility of not only traditional use as functional materials, but also the use of these materials for disinfection of surfaces, water and biological tissues.

Keywords: Erbium orthoniobate-orthotantalate; mechanical properties; photoluminescence; dark and photoinduced toxicity; Gram-positive; Gram-negative; spore-forming microorganisms

check for updates

Academic Editors: Letao Yang, Hua Hao, Qinghu Guo and Zhonghua Yao

Received: 16 September 2025
Revised: 13 October 2025
Accepted: 20 October 2025
Published: 22 October 2025

Citation: Palatnikov, M.; Shcherbina, O.; Fokina, N.; Smirnov, M.; Zelenina, E.; Masloboeva, S.; Manukovskaya, D. Erbium Orthoniobate-Tantalates: Structural, Luminescent and Mechanical Properties of $ErNb_xTa_{1-x}O_4$ Ceramics and Bactericidal Properties of $ErNbO_4$ Powder. *Ceramics* **2025**, *8*, 130. https://doi.org/10.3390/ceramics8040130

Copyright: © 2025 by the authors. Licensee MDPI, Basel, Switzerland. This article is an open access article distributed under the terms and conditions of the Creative Commons Attribution (CC BY) license (https://creativecommons.org/licenses/by/4.0/).

1. Introduction

The role of compounds and functional materials containing rare earth elements (REEs) in the development of modern technologies is constantly and inevitably increasing. The range of applications for such materials is expanding significantly. A huge amount of fundamental research is devoted to the design and characterization of luminescent materials that exhibit new photophysical effects [1–3]. The reason for this popularity is their role in modern technologies (display screens, optical communication amplifiers, LED lamps and solid-state lasers); the need for the materials is constantly growing.

Solid-state luminescent materials based on lanthanide niobate-tantalates $REE(Nb_xTa_{1-x})O_4$ have the combined advantages of typical lanthanide photoluminescence (PL) and photo-

physical stability. Lanthanide PL is known for two types of regimes: the conversion of exciting radiation is increased in one case, and it is decreased in the other case. Up-conversion luminescence (UCL) refers to a nonlinear optical process [3–5]. What is characteristic of this process? Two or more near-infrared (IR) photons are sequentially absorbed into several real intermediate energy states, and luminescence is emitted at a wavelength shorter than the wavelength of the absorbed radiation.

Trivalent REE niobate-tantalates, such as Er and Yb, have attracted much attention because these PL materials can convert near-IR excitation into visible emission, that is, they are up-conversion phosphors [4–6]. UCL arises from 4*f*-4*f* orbital electronic transitions with accompanying wave functions. They are localized within a single lanthanide ion. These internal 4*f* electronic transitions of lanthanide ions are largely electric-dipole transitions. They are prohibited by the selection rules. However, the rules are relaxed due to the local mixing of *f* states with higher electronic configurations. The local mixing itself is caused by the splitting of the crystal field levels [7–9]. Variation in the Nb/Ta ratio in $REE(Nb_xTa_{1-x})O_4$ increases energy transfer from the emission centers of the crystal host based on the TaO_4^{3-} and NbO_4^{3-} groups to the emission centers of REE cations.

Up-conversion phosphors are widely used in optical devices such as temperature sensors, IR quantum counters, and compact solid-state lasers [10]. However, converting near-IR to visible radiation eliminates background fluorescence and light scattering from biological materials. And this makes, in particular, micro-nano-grained up-conversion phosphors ideal for use in bioimaging with undeniable advantages, for example, the absence of autofluorescence of biological tissues and a large penetration depth [11]. However, the use of ABO_4-type compounds in medical practice requires preliminary biotesting and testing for toxicity, including in relation to various microorganisms [12].

It should also be noted that the phenomenon of resistance of pathogens to therapeutic drugs is the main reason for the negative effect on human health. This phenomenon is the basis for a sharp decrease in the effectiveness of etiotropic therapy for infectious diseases. The increasing resistance of microorganisms, on the one hand, to traditional antimicrobial drugs, and on the other hand, to traditional methods of chemical inactivation of bacteria makes the development of new effective methods for combating bacterial contamination and infections extremely relevant [13].

Finely dispersed powdered phosphors based on the compound $ErNbO_4$ emit over a wide range of the visible spectrum (~530–670 nm). They are almost insoluble in water in the temperature range −40–+100 °C, and are resistant to alkalis, acids and other aggressive environments. This markedly distinguishes them from organic and organometallic compounds. These properties also make it possible to use them in such conditions and situations where the chemical and temperature stability is important.

This significantly distinguishes them from organic and organometallic compounds used, for example, for antimicrobial photodynamic inactivation. And this expands the scope of its applications, for example, to the purification of industrial and agricultural wastewater, where the chemical and temperature stability of the bactericidal material is important [14–21].

Therefore, the urgent tasks for today are the following: first, the search for promising luminescent phosphors with UCL; secondly, the development of synthesis technology resulting in finely dispersed powders.

Such powders can be used in biology and medicine, including for antimicrobial photodynamic inactivation or bacteriotoxic light therapy (BLT) [14,15]. In addition, their use creates ceramic materials with increased hardness and strength, qualities necessary to produce a variety of sensors and counters, including those operating under conditions of increased mechanical loads.

The goal of this study is the synthesis of fine powders of erbium niobate-tantalates $ErNb_xTa_{1-x}O_4$ (x = 0; 0.1; 0.3; 0.5; 0.7; 0.9; 1); the preparation of ceramic samples and the study of their structural, mechanical and luminescent (up-conversion) characteristics; and also the study of the biological properties of $ErNbO_4$ powders, such as dark and photoinduced toxicity.

2. Methods

The synthesis of erbium niobate-tantalate powders $ErNb_xTa_{1-x}O_4$ (x = 0; 0.1; 0.3; 0.5; 0.7; 0.9; 1) was carried out using the liquid-phase method. The synthesis required high-purity fluoride Nb- and Ta-containing solutions or mixtures thereof. Their volumes provided the specified composition of niobate-tantalates. Solutions were prepared as follows: oxides Nb_2O_5 (99.9) and Ta_2O_5 (99.9) were dissolved in HF (99.9, Komponent-reaktiv Ltd., Moscow, Russia). Niobium, tantalum hydroxides or mixtures thereof were precipitated with 25% NH_4OH (99.9 (not more than 10^{-5} of 23 impurities), Sigma Tek, Khimki, Russia) from the initial solutions. Then, the sediment was washed three times using repulpation with deionized water to remove F^- ions at a ratio of solid (S) and liquid (L) phases $S:V_L$ =1:3, and dried at 100 °C. Then, a solution of $Er(NO_3)_3$ with a given concentration of Er at a ratio of $S:V_L$ =1:2 was added to the precipitate. Erbium nitrate solutions were prepared as follows: Er_2O_3 (oxide 99.9% LLC HimKraft, Moscow, Russia) was dissolved in HNO_3 (99.9, Vekton Ltd., Saint Petersburg, Russia). A 25% solution of NH_4OH (99, Sigma Tech, Khimki, Russia) at pH ~8–9 was introduced into the pulp formed during stirring. The precipitate was filtered and washed three times with deionized water at $S:V_L$ = 1:4 to remove ammonium ions, and then it was dried. The temperature was ~140 °C. Then, the sediment was calcined in a resistance furnace at 700 °C for 4 h. Then, the sediment was ground in a chalcedony ball mill (grinder) MLW KM1 (MLW, Leipzig, Germany). Then, the powders were calcined for 5 h at 1200 °C. The gravimetric method determined the content of niobium and tantalum in fluoride Nb- and Ta-containing solutions. The potentiometric method determined the content of fluoride ions in fluoride Nb- and Ta-containing solutions. An EV-74 ion meter with an F-selective electrode EVL-1M3 (Zavod izmeritel'nych priborov, Belarus, Gomel') was used as a research tool. Fluorine in the synthesized powders was analyzed by pyrohydrolysis. Erbium in filtrates and washing solutions was determined by inductively coupled plasma mass spectrometry (ICP-MS) ELAN 9000 DRC-e (PerkinElmer, Hopkinton, MA, USA). The elemental composition of the powders was evaluated by X-ray fluorescence spectrometry using a Spectroscan MAKC-GV (Spectron, Saint Petersburg, Russia).

The specific surface area of the powders was determined by the low-temperature nitrogen adsorption method (BET; FlowSorb II 2300; TriStar 3020 V1. 03, both from Micromeritics, Norcross, GA, USA). The average particle size of the powders d_{av} was determined from these data by the formula $d_{av} = 6/S_{sp} \cdot \rho$, where S_{sp} is the specific surface area, m^2/g; ρ is the density, g/cm^3.

X-ray phase analysis of the synthesized $ErNb_xTa_{1-x}O_4$ samples was performed on a Rigaku XtaLAB Synergy-S X-ray diffractometer (Rigaku, Tokyo, Japan) with a new generation PhotonJet-S multifocal source and an HPC detector (Rigaku, Tokyo, Japan). A Rietveld refinement was applied including Full Pattern Decomposition (FPD). The cell parameters of the ceramic solid solutions $ErNb_xTa_{1-x}O_4$ (x = 0; 0.1; 0.3; 0.5; 0.7; 0.9; 1) were refined by the WPPF (Whole Powder Pattern Fitting).

From powders obtained using conventional sintering (CS), ceramic samples were prepared in the form of tablets with a diameter of 10 mm and a height of 2–3 mm. Polyvinyl alcohol was the binder. The tablets were pressed at a load of ~3.8 kg/cm^2. The tablets

were sintered in a KEP 14/1400P electric furnace (MZVE LLC, Tryokhgorny, Russia). The temperature was 1400 °C, and the process lasted 3 h.

The multifunctional X-ray diffractometer Rigaku (RIGAKU, Japan, Tokyo) clarified the phase composition and structures of ceramic samples. The device is equipped with SmartLab Studio II software. The speed of the counter was 2 deg·min^{-1} (CuKα radiation, scanning range 6–90°). The ICDD (International Diffraction Data Center) databases (PDF 4, relies 2022) were used to identify the phases. The WPPF helped clarify the structural characteristics of the phases. Atomic coordinates and crystallographic lattice characteristics were entered from cif files ICDD. The R-factor criteria were the values of the profile agreement factors R_p and $R_{wp,}$ calculated using standard formulas.

A ZEISS EVO 25 UltimMax 170 scanning electron microscope SEM (Carl Zeiss QEC GmbH, Oberkochen, Germany) examined morphology and sizes of powders, as well as the microstructure of ceramic samples. Then, based on the SEM scans and the technical capabilities of the ScanMaster program (National research nuclear university (MEPHI), Moscow Engineering Physics Institute, Russia), we analyzed the obtained data. ScanMaster was created to mathematically process such images and measure them. The program is able to select objects in an image and perform morphological operations on them. It can calculate object characteristics based on selected criteria, perform statistical processing of a set of selected objects based on selected criteria and generate diagrams and correlations. The mechanical properties of ceramic samples (microhardness and Young's modulus) were studied by the contact method using a NanoSkan probe microscope-nanohardness tester (FSBI TISNCM, Troitsk, Russia). The methods were used from works [22–25]. The microhardness of ceramics was determined by comparative sclerometry [23], and Young's modulus was determined from approach curves [22]. The crack resistance, which is the stress intensity factor for mode I, $K_{IC,}$ was determined according to the model of Anstis et al. [24,25]. The load was 15 mN during the test. To reduce the standard error of the data, the obtained values of microhardness and crack resistance were averaged over ten measurements in 10 arbitrary areas measuring 60 × 60 μm for each sample.

PL spectra of the studied ceramics were obtained with an AvaSpec-3648 spectrofluorimeter (manufactured by Avantes, Apeldoorn, The Netherlands) when excited at a wavelength of 980 nm by a single-mode laser module KLM-H980 (PTI "Optronik", St. Petersburg, Russia) in the IR range with a continuous radiation power of 120/200 mW. The operating wavelength range of the spectrofluorimeter AvaSpec-3648 (Avantes BV, Apeldoorn, The Netherlands) is 330–980 nm with a resolution of 0.025 nm. The measurement step was 0.17 nm.

A total of three bacterial strains were used to determine the photoinduced and dark toxicity of $ErNbO_4$ powders. These are Gram-positive—*Micrococcus sp.* and Gram-negative—*Escherichia coli* strains. Another object was the spore-forming bacterium *Bacillus subtilis*. The studied strains were subcultured onto freshly prepared agar nutrient medium for research purposes; they were incubated in a thermostat at 27 °C for three days. To prepare a bacterial suspension, cultures were treated with sterile saline. The initial number of bacterial suspension was more than ~10^4 cells/mL. Photoinduced toxicity of $ErNbO_4$ powders was evaluated by the degree of inhibition of cell growth of three bacterial cultures under study in natural light. A sample of the material (2 or 5 mg/mL) was placed in a glass test tube containing 19 mL of saline solution, then 1 mL of bacterial suspension was added. A 2 mg sample was used for Gram-positive and Gram-negative bacteria, namely *Micrococcus sp.* and *Escherichia coli*, respectively; and a 5 mg sample was used for spore-forming bacteria Bacillus subtilis as they are more resistant to bactericidal substances. The test tube was tightly closed with a rubber sterile stopper and mounted on an orbital shaker LOIP LS-110 (LAB-PU-01) (JSC LOIP, Saint-Petersburg, Russia). The rotation speed was 200 rpm. The

test tube was kept in natural light for 24 h. The tubes were exposed to light during natural daylight hours. Sowing was carried out after 4 and 24 h.

The source of natural light was sunlight. A lux meter (TKA-PKM, 06) and a UV Radiometer (TU 4215-003-16796024-16) monitored the illumination level during the experiments. Luxmeter TKA-PKM (06) was produced by the Research and Production Enterprise "TKA", St. Petersburg, Russia. The illumination level of the samples in various spectral ranges is presented in Table 1.

Table 1. Illumination in the spectral range from 380 to 980 nm and irradiance in the spectral range from 280 to 400 nm.

Lighting Type	Illumination in the Spectral Range from ~400 to 980 nm, Lux	Energy Illumination in the Spectral Range from 280 to 400 nm, mW/m^2
Daylight	2617 ± 209	132 ± 13.2

Experiments in the dark were carried out to compare the results. They involved Gram-positive bacteria *Micrococcus sp*. Control experiments were carried out with the same lighting, but there were no luminescent phosphors in them. It has been found that the number of bacteria in the suspension does not significantly decrease over 4 and 24 h in natural light when there are no luminescent phosphors.

3. Results and Discussion

3.1. Dimensional Characteristics and Morphology of Powders

ICP-MS data indicate that, taking into account the volumes of solutions, the loss of erbium in filtrates and washing solutions is significantly less than 0.1 mg when synthesizing 30 g of powder for most of the studied samples. This means that gadolinium and europium are almost completely transferred from $Er(NO_3)_3$ solutions into the hydroxide precipitate. The data in Table 2 show that the concentrations of Er, Nb and Ta are close to the calculated values within the permissible error of the analysis method used (1%).

Table 2. Elemental composition and specific surface area of synthesized erbium niobate-tantalate powders.

Sample	Analysis Results, wt%			Specific Surface Area, S_{sp}, m^2/g	Average Particle Size of Powders d_{av}, μm
	Er	Nb	Ta		
$ErNbO_4$	50.40	29.62	-	1.04	0.78
$ErNb_{0.9}Ta_{0.1}O_4$	47.68	26.37	5.75	1.39	0.64
$ErNb_{0.7}Ta_{0.3}O_4$	46.22	19.40	15.89	1.28	0.56
$ErNb_{0.5}Ta_{0.5}O_4$	44.50	13.04	24.95	1.15	0.57
$ErNb_{0.3}Ta_{0.7}O_4$	41.65	7.53	34.07	1.54	0.42
$ErNb_{0.1}Ta_{0.9}O_4$	40.86	2.43	40.55	1.65	0.39
$ErTaO_4$	41.10	-	43.40	0.84	0.75

It has been found that the fluorine concentration in the powders is below the sensitivity limit of the analytical method used (less than 1×10^{-3}%).

Table 2 demonstrates that the average particle sizes of the powders in the series of studied compositions are quite similar. Therefore, we present a typical shape of the powders using a sample with the largest particle size $ErNbO_4$ and with the smallest particle size $ErNb_{0.1}Ta_{0.9}O_4$ as an example (Figure 1).

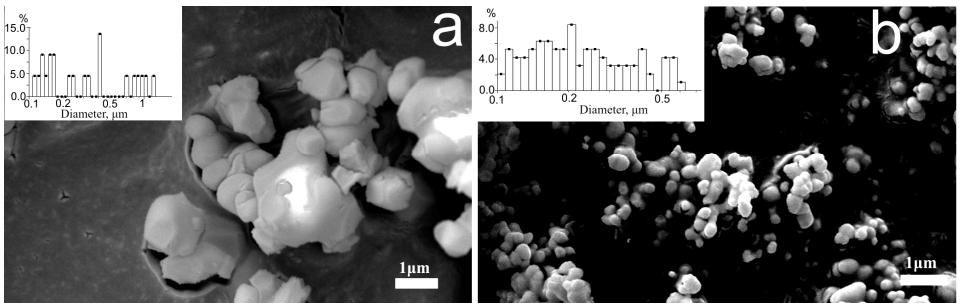


Figure 1. SEM images of $ErNb_xTa_{1-x}O_4$ powders of typical morphology: (**a**)—$ErNbO_4$; (**b**)—$ErNb_{0.1}Ta_{0.9}O_4$. The insets show differential particle size distribution curves.

Figure 1 shows that the powders consist of nearly spherical particles of similar morphology. The particle size of the $ErNbO_4$ powders ranges from 0.1 to 1.25 μm, as seen in Figure 1a. The average size of the $ErNb_{0.1}Ta_{0.9}O_4$ powders is ~0.1 to 0.7 μm, as seen in Figure 1b. It should be noted that the powder particles tend to stick together and form larger agglomerates.

3.2. Structure of Ceramic Solid Solutions

Figure 2 shows XRD patterns of $ErNb_xTa_{1-x}O_4$ samples (x = 0; 0.1; 0.3; 0.5; 0.7; 0.9; 1).

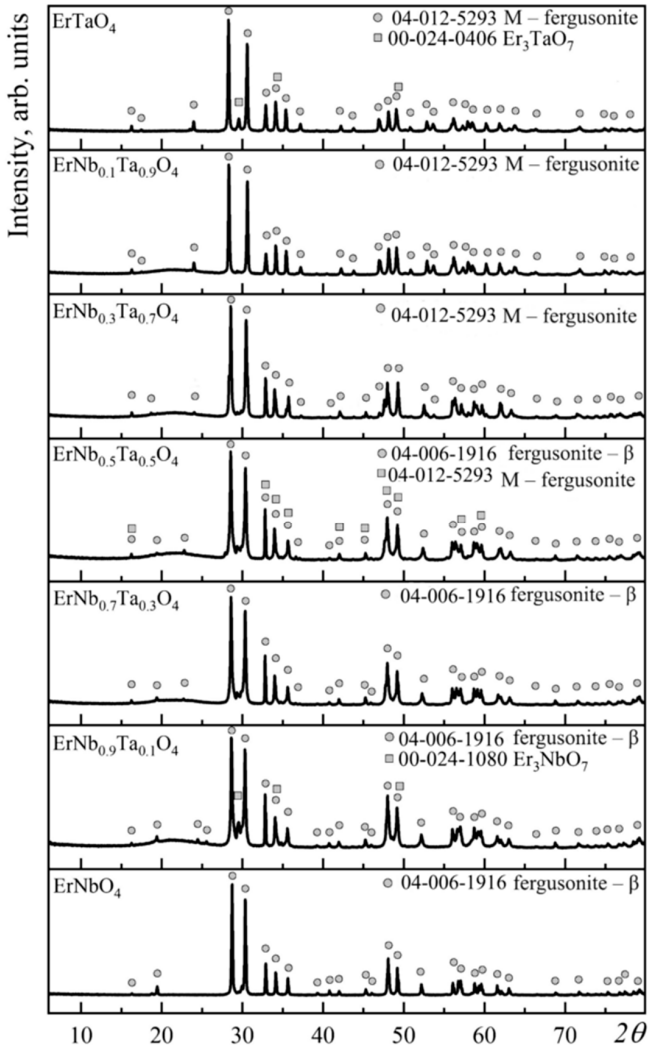


Figure 2. XRD patterns of $ErNb_xTa_{1-x}O_4$ ceramic samples with Rietveld refinement of the main phases.

Since the ionic radii of niobium and tantalum atoms in mixed orthoniobates-tantalates in the oxidation state of +5 and six-fold coordination are the same and equal to 0.64 Å [26], in accordance with the Goldschmidt tolerance factor, one can expect the formation of a continuous series of solid solutions $REENb_xTa_{1-x}O_4$ at x = 0–1. However, it was established that in the $ErNb_xTa_{1-x}O_4$ series, near x = 0.5, a structural transition occurs from the monoclinic symmetry of the C2/c cell to the monoclinic P2/a cell at the stage of FPD. The studied solid solutions $ErNb_xTa_{1-x}O_4$ at x = 0.5–1 crystallize in the structure of β-fergusonite with a monoclinic cell of erbium orthoniobate (ICDD, card 04-006-1916, space group (SPGR): C2/c (15) Z = 4), and at $x \leq 0.5$ in the form of M-fergusonite erbium orthotantalate (ICDD, card 04-012-5293, SPGR: P2/a (13), Z = 2). The cell parameters of $ErNb_xTa_{1-x}O_4$ (x = 0; 0.1; 0.3; 0.5; 0.7; 0.9; 1) refined by the WPPF method are presented in Table 3. It should be noted that in the $ErNb_xTa_{1-x}O_4$ sample, at x = 0.5, two phases were identified simultaneously: about 82% monoclinic β-fergusonite with the SPGR C2/c and 18% monoclinic M-fergusonite with P2/a. The concentration region around the point Nb/Ta = 1 in the series of solid solutions $ErNb_xTa_{1-x}O_4$ is probably a morphotropic region of coexistence of two phases of fergusonite.

Table 3. Refined values of the periods of unit cells of the main phases of ceramic samples $ErNb_xTa_{1-x}O_4$ (x = 0; 0.1; 0.3; 0.5; 0.7; 0.9; 1).

Sample Composition	Phase in the Sample	*a*, Å	*b*, Å	*c*, Å	β, °	V	R_{wp}, %	R_p, %
$ErNbO_4$	04-006-1916 SPGR: C2/c (15) $ErNbO_4$	7.02557(8)	10.91922(14)	5.06648(7)	131.4512(6)	291.315	7.49	5.67
$ErNb_{0.9}Ta_{0.1}O_4$	04-006-1916 SPGR: C2/c (15) $ErNbO_4$	7.0183(3)	10.9163(4)	5.0642(2)	131.390(2)	291.077	10.19	5.96
$ErNb_{0.7}Ta_{0.3}O_4$	04-006-1916 SPGR: C2/c (15) $ErNbO_4$	7.0040(3)	10.9126(4)	5.0592(2)	131.1898(19)	290.992	8.68	5.32
$ErNb_{0.5}Ta_{0.5}O_4$	04-006-1916 SPGR: C2/c (15) $ErNbO_4$ Phase weight 82%	6.9911(2)	10.9080(4)	5.05474(19)	131.0188(18)	290.836	6.08	4.01
	04-012-5293; $ErTaO_4$ P2/a (13) Phase weight 18%	5.3035(4)	5.4538(4)	5.1333(6)	96.100(8)	147.639	6.08	4.01
$ErNb_{0.3}Ta_{0.7}O_4$	04-012-5293, $ErTaO_4$ P2/a (13)	5.2996(3)	5.4523(3)	5.0550(3)	95.276(2)	145.446	10.00	6.72
$ErNb_{0.1}Ta_{0.9}O_4$	04-012-5293, $ErTaO_4$ P2/a (13) M	5.28439(11)	5.44368(11)	5.09790(10)	96.3053(8)	145.762	4.63	3.35
$ErTaO_4$	04-012-5293, $ErTaO_4$ P2/a (13) M	5.2827(3)	5.4402(3)	5.0981(3)	96.352(3)	145.614	6.42	4.73

Figure 3 shows the structures of the monoclinic cells P2/a and C2/c and their corresponding coordination polyhedra. The differences lie in the anionic composition.

It is believed that the coordination polyhedron around the Ta atoms for the P2/a cell can be fairly interpreted as a tetrahedron (semi-dodecahedron) (4 + 2), and for the C2/c cell and Nb atoms, it can be fairly interpreted as a distorted octahedron [27]. Moreover, the additional O atoms in the case of C2/c (β-fergusonite) are closer to the atoms of the cation sublattice A^{5+} than in M-fergusonite with the P2/a cell (Figure 3, Table 4). In the structure of β-fergusonite, the atoms of the crystalline host (tantalum or niobium) are in a strongly distorted octahedral coordination with six Ta(Nb)–O bonds whereas in M-fergusonite the tantalum (niobium) atoms are in a tetrahedral coordination; see Figure 3.

The cell parameters increase with increasing Nb content in the host (see Table 3) due to the increase in distances between A^{5+} and oxygen ions (Table 4).

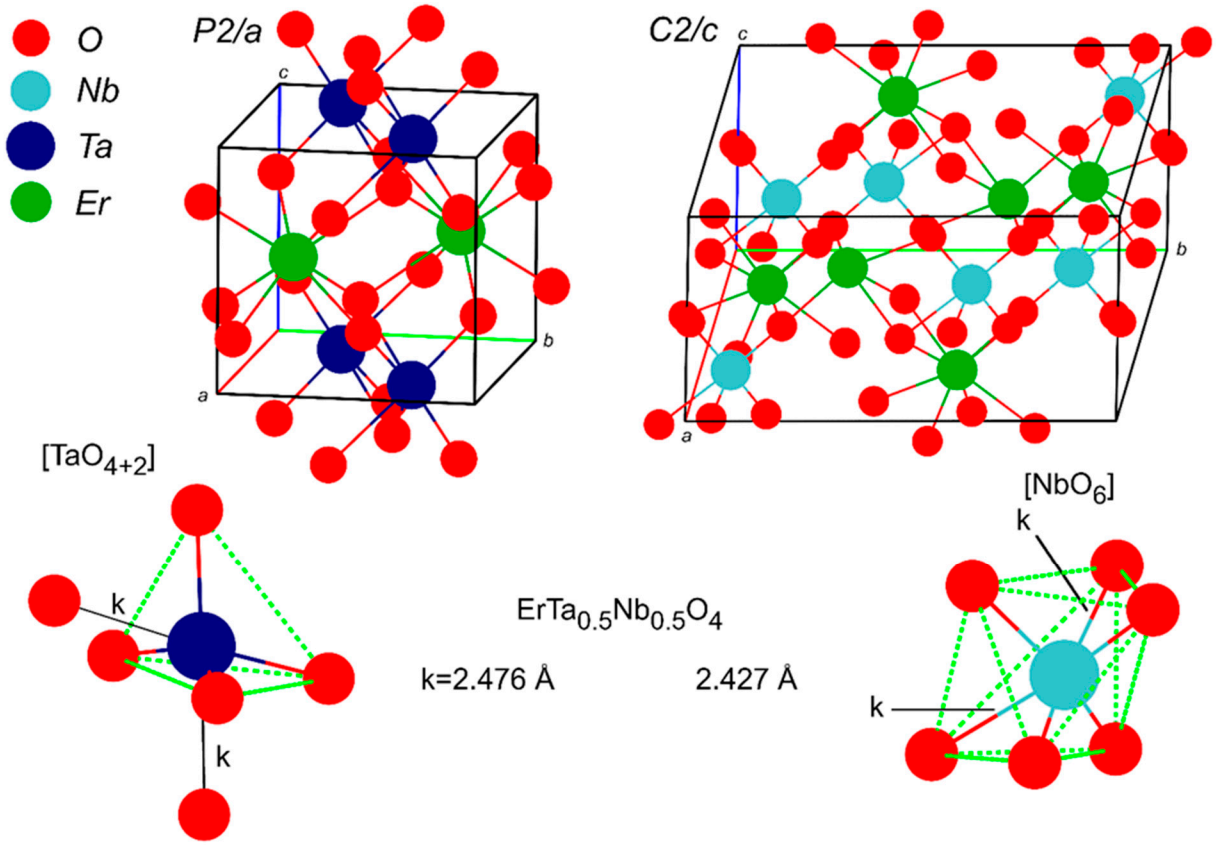


Figure 3. Structure of monoclinic cells P2/a and C2/c and coordination polyhedra around Ta and Nb atoms, respectively. The figure shows the distances *k* from the atoms of the crystal host (A^{5+}) to the most distant oxygen atoms in the cell.

Table 4. Interatomic distances between A^{5+} and O^{2-} ions in $ErNb_xTa_{1-x}O_4$ (x = 0; 0.1; 0.3; 0.5; 0.7; 0.9; 1).

SPGR	Distance	Nb Content, x						
		1	0.9	0.7	0.5	0.3	0.1	0
C2/c (15), Z = 4	$Nb–O(1)_a[O(1)_b]$	1.76588	1.76454	1.76171	1.75912			
	$Nb–O(2)_a[O(2)_b]$	2.42890	2.42703	2.42326	2.41979			
	$Nb–O(2)_c[O(2)d]$	1.82574	1.82646	1.82990	1.83271			
P2/a (13), Z = 2	$Ta–O(1)_a[O(1)_b]$				1.92793	1.92689	1.91520	1.91407
	$Ta–O(1)_a[O(1)_b]$				2.48018	2.45572	2.47252	2.47237
	$Ta–O(2)c[O(2)_d]$				1.99687	1.97556	1.98987	1.98973

This pattern is probably due to the different electronegativity of Ta (1.5 on the Pauling scale) and Nb (1.6 on the Pauling scale) and, as a consequence, the different effective charges on the Ta^{5+}, Nb^{5+} and O^{2-} ions in compounds with a covalent bond [28]. In the case of TaO_6^- or NbO_6^- groups, a small increase in the electronegativity of the cation from Ta^{5+} to Nb^{5+} is accompanied by an increase in the ionic radius of O^{2-}. These changes probably lead to an increase in the length of the A^{5+}–O^{2-} bonds.

Deviations in the lattice constants from Vegard's law are explained, as in work [29], by the formation of inhomogeneities (clusters) enriched with one of the substituted atoms.

In addition, the $ErTaO_4$ sample contains about 6 wt% Er_3TaO_7 cubic system with Fm-3m (225) (ICDD, card 00-024-0406), and the $ErNb_{0.9}Ta_{0.1}O_4$ ceramic sample contains about 10 wt% cubic Er_3NbO_7 (ICDD, card 00-024-1080, SPGR: Fm-3m) (Figure 2, Table 3).

3.3. Morphological and Mechanical Characteristics of Ceramic Solid Solutions $ErNb_xTa_{1-x}O_4$ (x = 0; 0.1; 0.3; 0.5; 0.7; 0.9; 1)

A series of SEM images were performed to characterize the morphologies and estimate the grain sizes of $ErNb_xTa_{1-x}O_4$ (x = 0; 0.1; 0.3; 0.5; 0.7; 0.9; 1). The microstructure of ceramic samples and their size composition are shown in Figure 4.

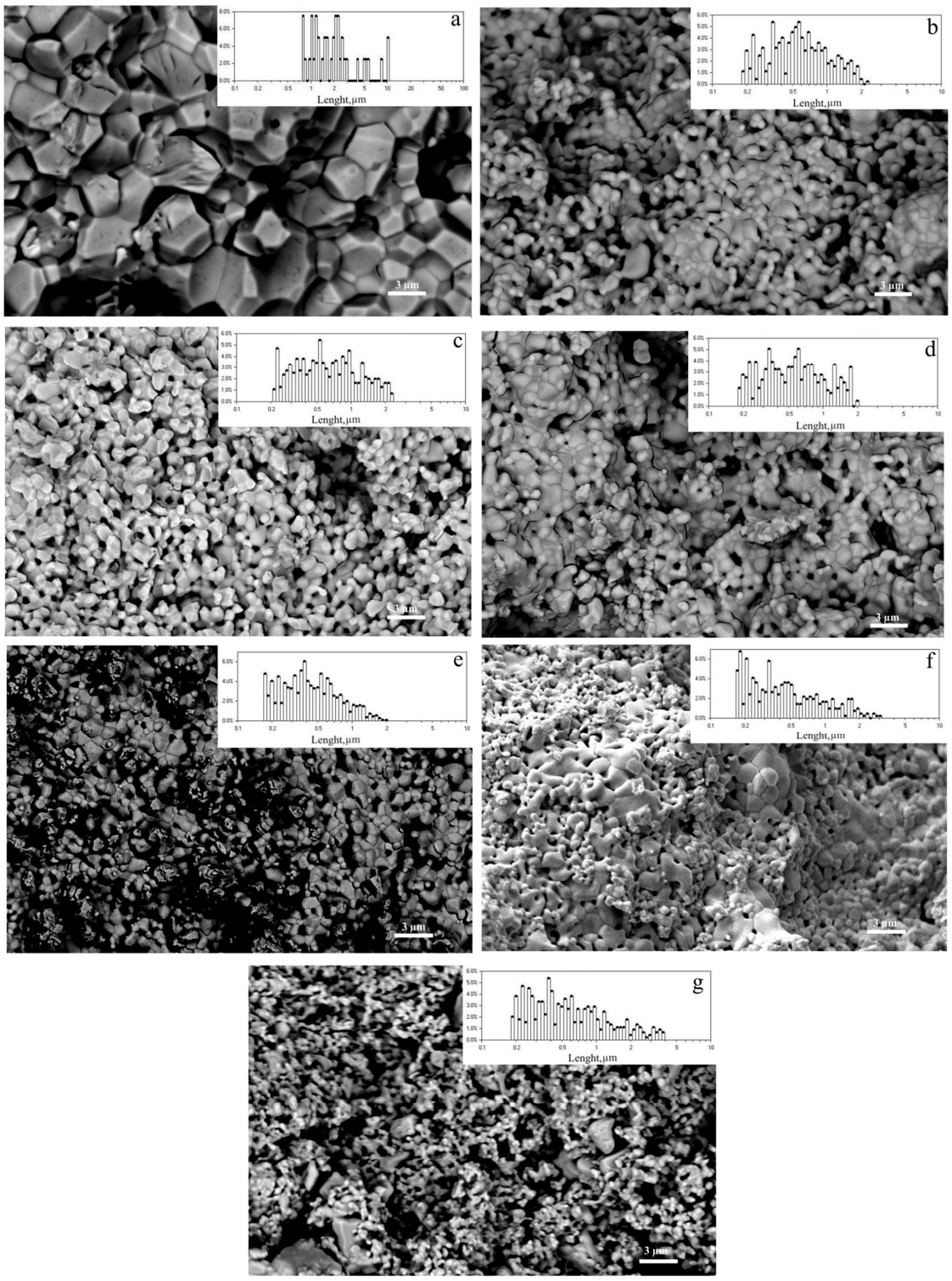


Figure 4. Microstructure and size composition of crystallites (in inserts) of $ErNb_xTa_{1-x}O_4$ ceramic samples: (**a**) $ErNbO_4$; (**b**) x = 0.9; (**c**) x = 0.7; (**d**) x = 0.5; (**e**) x = 0.3; (**f**) x = 0.1; (**g**) $ErTaO_4$.

The data in Figure 4 show that $ErNb_xTa_{1-x}O_4$ ceramic samples consist of grains of similar morphology with pronounced boundaries. The largest crystallite size is in the $ErNbO_4$ sample, from ~0.7 to ~10 μm, as seen in Figure 4a. It is likely that the large grain size of $ErNbO_4$ ceramics may be due to the sintering temperature of the ceramics. It is close to the melting point.

If Ta in the $ErNb_xTa_{1-x}O_4$ composition increases, respectively, and the melting temperature increases, the ceramic grain size decreases. The range of crystallites from ~ 0.2 to ~ 2.6 μm is typical for the $ErNb_{0.9}Ta_{0.1}O_4$ and $ErNb_{0.7}Ta_{0.3}O_4$ samples, as seen in Figure 4b,c. The size of the main fraction of crystallites is from ~0.18 to ~2.2 μm for $ErNb_xTa_{1-x}O_4$ ceramics, where $x \leq 0.5$, as seen in Figure 4d–g. Ceramic samples $ErNb_{0.9}Ta_{0.1}O_4$ and $ErTaO_4$ containing cubic phases with Fm-3m (225) Er_3NbO_7 and Er_3TaO_7, respectively, (Figure 4b,g) are the most heterogeneous and contain individual grains larger than 3.0 μm. In general, $ErNb_xTa_{1-x}O_4$ ceramics (x = 0; 0.1; 0.3; 0.5; 0.7; 0.9; 1) prepared by CS from erbium niobate-tantalate powders synthesized by the liquid-phase method have a finer grain size than those obtained by solid-phase synthesis with crystallite sizes about or more than 5.0 μm [30–33].

The contact method helped to study the mechanical properties of ceramic samples. Table 5 shows the results of measurements and calculations of the mechanical characteristics of ceramic samples.

Table 5. Mechanical characteristics of $ErNb_xTa_{1-x}O_4$ ceramic samples.

Sample Composition	Microhardness, H, GPa	Young's Modulus, E, GPa	Crack Resistance, K_{IC}, MPa m$^{0.5}$
$ErNbO_4$	6.11 ± 0.86	297.6 ± 10.8	1.44 ± 0.2
$ErNb_{0.9}Ta_{0.1}O_4$	2.86 ± 0.31	84.8 ± 1.8	0.7 ± 0.1
$ErNb_{0.7}Ta_{0.3}O_4$	5.68 ± 1.0	162.4 ± 6.9	1.20 ± 0.1
$ErNb_{0.5}Ta_{0.5}O_4$	3.82 ± 0.33	137.7 ± 4.3	1.10 ± 0.1
$ErNb_{0.3}Ta_{0.7}O_4$	5.12 ± 1.1	223.1 ± 5.9	1.16 ± 0.15
$ErNb_{0.1}Ta_{0.9}O_4$	3.4 ± 0.361	98.8 ± 2.7	0.94 ± 0.1
$ErTaO_4$	4.2 ± 0.9	139.3 ± 6.8	1.06 ± 0.1

The data in Table 5 show that the mechanical characteristics of ceramics strongly depend on the phase composition of the samples. The best mechanical characteristics, microhardness (H = 6.11 ± 0.86 GPa), Young's modulus (E = 297.6 ± 10.8 GPa) and crack resistance (K_{IC} = 1.44 ± 0.2, MPa m$^{0.5}$) are found in the $ErNbO_4$ ceramic sample and the $ErNb_{0.7}Ta_{0.3}O_4$ single-phase sample, as seen in Figure 2, Table 3. Low mechanical characteristics of the $ErNb_{0.5}Ta_{0.5}O_4$ sample are due to the coexistence of two fergusonite phases. The low mechanical characteristics of the $ErNb_{0.9}Ta_{0.1}O_4$ sample are naturally due to the presence in the sample of about 10 wt% cubic Er_3NbO_7 phase (ICDD, card 00-024-1080, SPGR: Fm-3m). The key parameters in the difference in the mechanical characteristics of the compared orthoniobate-tantalates are the method of obtaining the materials, the properties and concentration of doping REEs and the ratio of crystalline phases in the sample. Nevertheless, the values of the mechanical characteristics of $ErNb_{1-x}Ta_xO_4$ ceramic samples synthesized by the liquid-phase method are consistent with the results presented in the literature [30–33]. The authors of [31,32] show the range of Young's modulus for REE-niobates ($RENbO_4$) (RE = Y, La, Nd, Sm, Gd, Dy, Yb)—60-170 GPa and hardness up to 11.48 GPa. The values of Young's modulus ~120 GPa for $YbTaO_4$ and $LuTaO_4$, ~270 GPa for $ScTaO_4$ are presented in [33]. Taking into account the differences in measurement methods (nanoindentation and sclerometry), our results of measuring these quantities are in a good agreement with the data in the literature. For example, the Young's modulus of $RENbO_4$ ceramics decreases linearly as the ionic radius of RE^{3+} increases [31,32]. The ionic radius of Er^{3+} is smaller than the ionic radii of Sm^{3+}, Gd^{3+}, Dy^{3+}; therefore, it is natural

that the single-phase ceramic sample $ErNbO_4$ has higher mechanical characteristics than orthoniobates Sm^{3+}, Gd^{3+} and Dy^{3+}. The latter are considered by the authors of [31,32].

3.4. Study of PL of Ceramic Solid Solutions $ErNb_xTa_{1-x}O_4$ (x = 0; 0.1; 0.3; 0.5; 0.7; 0.9; 1)

Figure 5 shows the PL spectra of $ErNb_xTa_{1-x}O_4$ ceramics when laser radiation excites the near-IR range (λ_{exc} = 980 nm). The PL spectra of the samples under study consist of bands of different intensities which depend on the composition of the ceramics. The PL bands correspond to intraconfigurational transitions of the Er^{3+} ion in the host of ceramic samples in the spectral range from 500 to 700 nm. For example, the main radiative transitions of the Er^{3+} ion correspond to ($^2H_{11/2}$, $^4S_{3/2}$) → $^4I_{15/2}$ in the region of 500–560 nm and the main radiative transitions of the Er^{3+} ion correspond to $^4F_{9/2}$ → $^4I_{15/2}$ in the region of 640–680 nm [34–36], as seen in Figure 5. PL peaks at 585 and 594 nm and, as far as we know, have not been previously observed in ceramic and single-crystalline niobate-tantalates of alkali and REEs [35,36]. The reason for the appearance of these bands can presumably be associated with the radiative transition $^4G_{9/2}$ → $^4I_{11/2}$ of the Er^{3+} ion during three-photon absorption according to the refined Dieke's diagram [34].

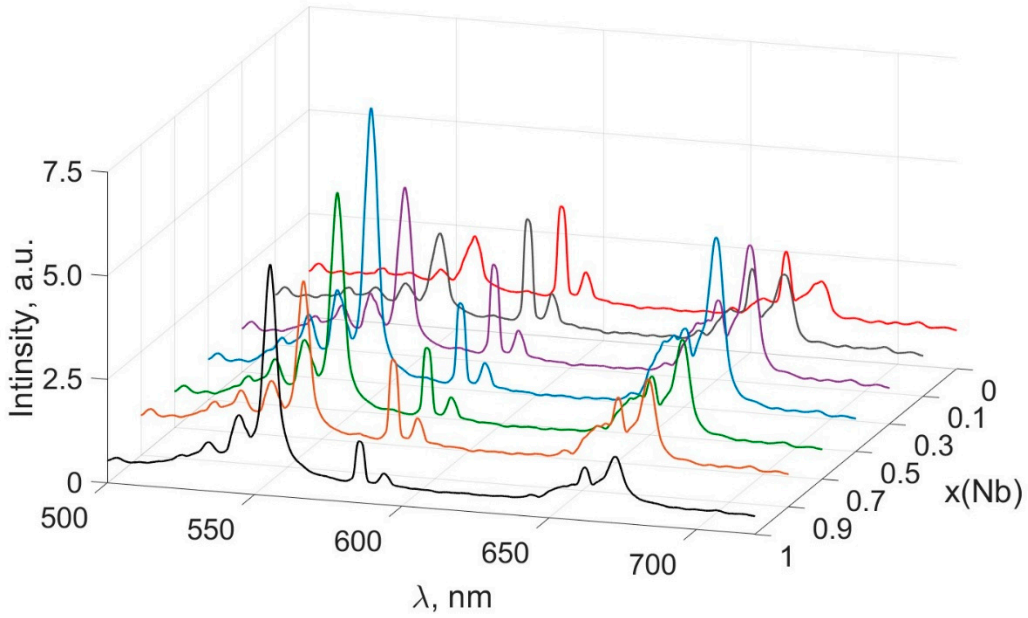


Figure 5. UCL spectra of $ErNb_xTa_{1-x}O_4$ ceramics excited by near-IR laser radiation.

The mechanism of UCL of the Er^{3+} ion consists of sequential absorption of IR radiation and subsequent emission in the visible region. Initially, the first low-energy quantum with energy E_{exc} = 1.27 eV is absorbed by the Er^{3+} ion and transferred to the excited state (transition $^4I_{15/2}$ → $^4I_{11/2}$). Subsequent absorption of the second quantum transfers the Er^{3+} ion to a higher energy state. This increases the population of the $^4F_{7/2}$ levels.

Further nonradiative recombination with the participation of lattice phonons transfers the Er^{3+} ion to the $^4S_{3/2}$ state. The radiative transition $^4S_{3/2}$ →$^4I_{15/2}$ produces UCL in the visible region. The radiative transition $^2H_{11/2}$ → $^4I_{15/2}$ (Figure 5 appears in the PL spectra near 535 nm due to the small energy difference between the $^2H_{11/2}$ and $^4S_{3/2}$ levels and the influence of the crystal field of the ceramic host [34–38].

The transition of the Er^{3+} ion to the $^4F_{9/2}$ state is possible in two ways. The first is phonon relaxation from the $^4S_{3/2}$ level to the $^4F_{9/2}$ level. However, this transition has a low probability as the intensity of the radiative transition $^4F_{9/2}$ → $^4I_{15/2}$ is extremely low when the UV region is excited, compared to that when the near-IR region is excited [37]. The second way involves nonradiative relaxation from the $^4I_{11/2}$ level to $^4I_{13/2}$ and subsequent

absorption of exciting radiation ($^4I_{13/2} \rightarrow {}^4F_{9/2}$ transition). The latter provides intense PL at 675 nm, as seen in Figure 5. The transfer of the Er^{3+} ion to the excited state $^4F_{7/2}$ is also possible due to the resonant energy transfer between two REEs where one element is a sensitizer, the second is an activator [39].

The highest quantum yield of PL is observed in $ErNbO_4$ ceramics in comparison with $ErTaO_4$ in individual compounds. The excess in intensity of the $^4S_{3/2} \rightarrow {}^4I_{15/2}$ transition is about 60%, as seen in Figure 5. One of the reasons for the weak intensity of UCL of $ErTaO_4$ ceramics may be due to the presence of an additional phase in the form of Er_3NbO_7 (cubic system, Figure 2, Table 3). It leads to the creation of structural defects of various sizes at the boundaries of two phases. The latter can lead to an increase in the proportion of nonradiative processes and weak PL intensity of Er^{3+} ions in the $ErTaO_4$ host. The PL intensity in the green and red regions of the spectrum depends on the Nb/Ta ratio in mixed ceramic matrices.

Changing the Nb/Ta ratio changes the average distance between the atoms of the crystal host (A^{5+}) and O^{2-} (Table 4). This can cause PL quenching in the tantalate host [40,41]. Substitution of Nb^{5+}/Ta^{5+} in the solid solution also leads to changes in the crystal field strength due to a change in the lengths of the A^{5+}–O^{2-} bonds. The atom substitution affects the symmetry of the local environment of the luminescence center. Both of these quantities affect the host element of the transition between the ground and excited states of the ion and the shape of the vibronic potential and change the PL intensity.

Figure 6 shows the change in the intensity of the peaks at 555 and 672 nm in the samples depending on the composition. If there is a gradual decrease in Nb from $x = 1$ to $x = 0.5$, the PL intensity at 555 and 672 nm increases in $ErNb_{x-1}Ta_xO_4$ ceramics, with the exception of ceramics with the composition $ErNb_{0.9}Ta_{0.1}O_4$. According to X-ray phase analysis, an additional phase Er_3NbO_7 (see Figure 2, Table 3) is present in the last sample. This phase reduces the PL intensity to the greatest extent at 555 nm. When the amounts of Nb and Ta in the $ErNb_{0.5}Ta_{0.5}O_4$ ceramic structure are equal, the PL intensity of both maxima reaches its maximum value. And this intensity prevails over the PL intensity in individual compounds. This may be promising for creating temperature sensors based on this material [35,37,38].

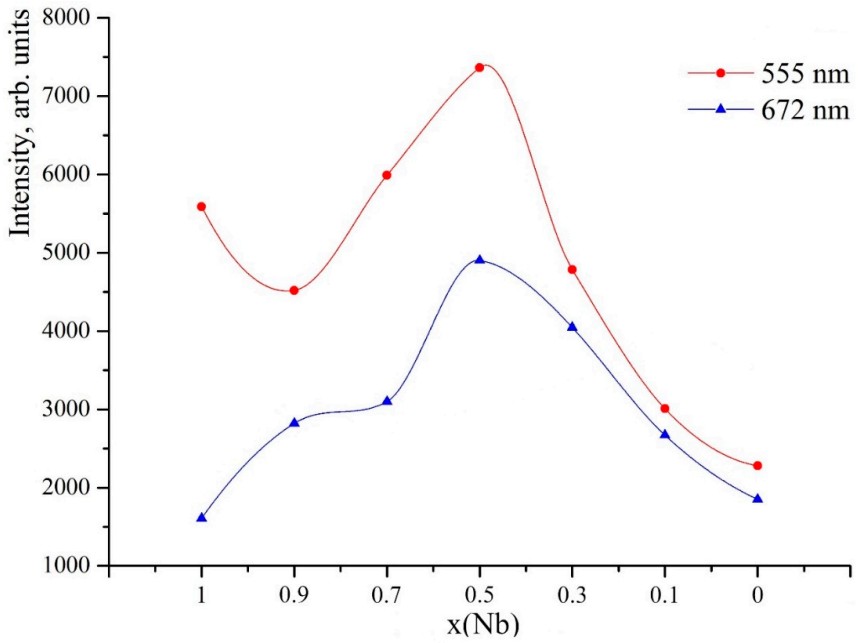


Figure 6. Change in the intensity of the main bands of the PL spectrum of $ErNb_{1-x}Ta_xO_4$ ceramics depending on the composition.

These results correlate well with the presence of two phases in the sample with the composition $ErNb_{0.5}Ta_{0.5}O_4$—about 82% monoclinic β-fergusonite with C2/c and 18% monoclinic M-fergusonite with P2/a. An increase in the PL intensity is observed in the region around Nb/Ta = 1. This may be due to the structural rearrangement of one cell into another. This in turn affects the efficiency of Er PL due to anisotropic changes in the distance between the ErO_8 polyhedron and neighboring AO_6.

The intensity of the PL bands at 585 and 594 nm monotonically increases in the series of $ErNbO_4$ →$ErNb_{0.7}Ta_{0.3}O_4$ →$ErNb_{0.5}Ta_{0.5}O_4$ ceramics, which are monophasic with a fergusonite-β type structure, as seen in Figure 2.

The main energy process in the studied $ErNb_xTa_{1-x}O_4$ ceramics is the energy transfer from the host. At the same time, there is a general tendency of increasing PL intensity in the blue region of the spectrum in $ErNb_xTa_{1-x}O_4$ with increasing niobium concentration [42]. If there were no disorder processes in the niobium-tantalum sublattice, the growth of PL intensity (I) with increasing niobium concentration (x) would proceed without anomalies and the dependence $I(x)$ would be close to linear. However, due to the structural transition from the monoclinic symmetry of the C2/c cell to the monoclinic P2/a cell and the positional disorder of the niobium and tantalum cations near the concentration x = 0.5, a pronounced maximum is observed in the $I(x)$ dependence.

When the niobium concentration increases in the range x = 0.5–0.7, the positional disorder in the B-sublattice decreases and the polarization of the oxygen octahedron AO_6 changes (Table 4); a regular decrease in the PL intensity is also observed.

At further increase in niobium concentration (x = 0.7–1.0), the tendency of the intrinsic PL intensity growth in $ErNb_xTa_{1-x}O_4$ with increasing niobium concentration comes into force [42]. That is, the energy transfer from the $ErNb_xTa_{1-x}O_4$ host to Er^{3+} increases and, accordingly, the PL intensity at the intracenter transitions of Er^{3+} ion grows.

3.5. Bacteriological Properties of Powder $ErNbO_4$

To test the photobactericidal properties, a simple composition, $ErNbO_4$, which has moderate luminescent properties, was chosen,. In experiments made to test photoinduced toxicity under natural light, luminescent powder $ErNbO_4$ showed good bactericidal action against bacterial cells of *Escherichia coli*, *Bacillus brevis* and *Micrococcus sp.* The residual number of bacteria after exposure for 24 h was ~20.6, 16.94 and 11.67%, respectively, of the initial value, as seen in Table 6.

Table 6. Change in the number of bacterial cells in the sample depending on the exposure time under natural light in the presence of $ErNbO_4$ powder. $ErNbO_4$ concentration—2 and 5 (*Bacillus brevis*) mg/mL.

Sample	Bacterial Cell Type	Number of Bacterial Cells					
		Initial		in 4 h		in 24 h	
		$\times 10^4$ cells/mL	%	$\times 10^4$ cells/mL	%	$\times 10^4$ cells/mL	%
1	*Escherichia coli*	6 ± 0.4	100	1.2 ± 0.5	20.3	1.2 ± 0.018	20.6
2	*Bacillus brevis*	6 ± 0.4	100	1.5 ± 0.19	25.0	1 ± 0.2	16.94
3	*Micrococcus sp.*	6 ± 0.4	100	1.25 ± 0.75	20.8	0.7 ± 0.01	11.67

The most resistant to the effect were Gram-negative bacterial cells *Escherichia coli*, as seen in Table 6. This is due to the more complex structure of their cell wall compared to Gram-positive *Micrococcus sp.* It is generally known that the main structure responsible for the general resistance of Gram-negative bacteria to various external agents is the outer membrane. It is part of the cell wall [43]. The outer membrane is based on a two-layer asymmetric structure. Their outer layer consists mainly of liposaccharides (LPS) and protein

complexes embedded between LPS [44]. The total negative charge of LPS is associated with a high content of negatively charged groups in the central part of these macromolecules.

Probably, under the influence of the polycationic compound $ErNbO_4$, LPS are released, disintegration of the outer membrane occurs and its permeability increases [45,46].

Gram-positive bacterial cells *Micrococcus sp.* participated in experiments without lighting. Experiments have shown that the number of bacterial cells *Micrococcus sp.* decreases only by half when they are kept in the dark. This is apparently due to the insignificant bactericidal activity of $ErNbO_4$ itself, Table 7.

Table 7. Change in the number of bacterial cells of *Micrococcus sp.* under natural light and in the dark, in the presence of $ErNbO_4$ powder. The concentration of $ErNbO_4$ is 2 mg/mL.

Bacterial Cell Type	Experimental Conditions	Number of Bacterial Cells					
		Initial		in 4 h		in 24 h	
		$\times 10^5$ cells/mL	%	$\times 10^5$ cells/mL	%	$\times 10^5$ cells/mL	%
Micrococcus sp.	light	1.41 ± 0.5	100	0.29 ± 0.18	20.6	0.16 ± 0.02	11.35
	dark	1.41 ± 0.5	100	0.7 ± 0.3	49.65	0.7 ± 0.01	49.65

Table 7 shows that in the dark, the number of bacterial cells *Micrococcus sp.* in the presence of $ErNbO_4$ phosphor powder decreases significantly less and more slowly than in natural light.

Photoinduced toxicity of $ErNbO_4$ applied to bacterial cells of *Micrococcus sp.* is higher than dark toxicity by ~5 times. Photoinduced toxicity of the $ErNbO_4$ luminophore is most effective for inactivating bacterial cells *Micrococcus sp.* Their distinctive feature is the simple structure of the cell wall. It should also be noted that the experimental results are very reproducible. Experiments in light with bacterial cells *Micrococcus sp.* were repeated in a comparative series of experiments in light and in the dark. The residual amount of *Micrococcus sp.* after exposure for 24 h in the first experiment was 11.67%, and it was 11.35% under the same conditions in the second, as seen in Tables 6 and 7. Thus, the results coincide within the experimental error.

4. Conclusions

The liquid-phase synthesis method using erbium nitrate solutions and co-precipitated niobium and tantalum hydroxides helped to obtain fine powders of erbium niobate-tantalates $ErNb_xTa_{1-x}O_4$ (x = 0; 0.1; 0.3; 0.5; 0.7; 0.9; 1)

Ceramic samples were prepared from the resulting fine powders, according to CS. The phase structures of $ErNb_{1-x}Ta_xO_4$ ceramic solid solutions depending on the Nb/Ta ratio in the composition of the samples were obtained by Rietveld refinement of X-ray diffraction patterns of polycrystals. It has been shown that the structure of the $ErNb_xTa_{1-x}O_4$ solid solution from x = 1 to x = 0.5 corresponds to the structure of fergusonite-β with a monoclinic cell of erbium orthoniobate (ICDD, card 04-006-1916 SPGR: C2/c (15), Z = 4).

It has been established that in the $ErNb_xTa_{1-x}O_4$ series, at about x = 0.5, a structural transition occurs from the monoclinic symmetry of the C2/c cell to the monoclinic P2/a cell. When Ta in $ErNb_xTa_{1-x}O_4$ increases (at x = 0.3 or less), the solid solution crystallizes in the structure of M-fergusonite, ICDD, card 04-012-5293 SPGR: P2/a (13), Z = 2. The crystal matrix atoms (tantalum or niobium) are in a distorted octahedral coordination with six Ta(Nb)–O bonds in the β-fergusonite structure, and the tantalum (niobium) atoms are in a tetrahedral coordination in M-fergusonite.

The mechanical characteristics of ceramic solid $ErNb_xTa_{1-x}O_4$ (x = 0; 0.1; 0.3; 0.5; 0.7; 0.9; 1) solutions were determined. It was shown that the best mechanical characteristics, microhardness (H = 6.11 ± 0.86 GPa), Young's modulus (E = 297.6 ± 10.8 GPa) and

crack resistance (K_{IC} = 1.44 ± 0.2, MPa $m^{0.5}$) were possessed by the $ErNbO_4$ ceramic sample and the single-phase niobate-tantalate sample $ErNb_{0.7}Ta_{0.3}O_4$ with microhardness (H = 5.68 ± 1.0 GPa), Young's modulus (E = 162.4 ± 6.9 GPa) and crack resistance (K_{IC} = 1.20 ± 0.1 MPa $m^{0.5}$).

The luminescent properties of ceramic samples were studied. It was shown that when laser radiation excites in the near-IR range (λ_{exc} = 980 nm), solid solutions of $ErNb_xTa_{1-x}O_4$ (x = 0; 0.1; 0.3; 0.5; 0.7; 0.9; 1) irradiate PL with increasing conversion of the exciting radiation, and maximum value of PL was in $ErNb_{0.5}Ta_{0.5}O_4$.

The photoinduced and dark toxicity of the up-conversion phosphor $ErNbO_4$ was studied in relation to Gram-positive, Gram-negative and spore-forming microorganisms. It was shown that inactivation of Gram-positive bacteria *Micrococcus sp.* by the up-conversion phosphor $ErNbO_4$ is most effective in the light. This is apparently due to the structure of their cell wall.

Author Contributions: Conceptualization—O.S., M.P. and N.F.; Methodology—O.S., M.S., E.Z. and N.F.; Validation—M.S., O.S. and N.F.; Investigation—S.M., O.S., M.S., E.Z. and N.F.; Data Curation—E.Z. and S.M.; Writing—Original Draft—O.S., M.S., S.M., N.F. and D.M.; Writing—Review and Editing—O.S. and M.P.; Visualization—O.S., M.S. and N.F.; Resources—D.M.; Supervision—O.S. All authors have read and agreed to the published version of the manuscript.

Funding: This work was financially supported by the Ministry of Science and Higher Education Russian Federation scientific topics FMEZ-2025-0055 and FMEZ-2025-0044.

Data Availability Statement: Data is provided within the manuscript and will be available from the corresponding author on a reasonable request.

Conflicts of Interest: The authors declare no conflicts of interest.

References

1. Ikesue, A. (Ed.) Solid-State Lighting. In *Processing of Ceramics Breakthroughs in Optical Materials*; Wiley: Hoboken, NJ, USA, 2021; pp. 187–274.
2. Li, W.; Mi, W.; Chen, L.-J. Advances, challenges and prospects of visible fiber lasers in display technologies. *Displays* **2024**, *82*, 102630. [CrossRef]
3. Auzel, F. Upconversion and anti-stokes processes with f and d ions in solids. *Chem. Rev.* **2004**, *104*, 139–174. [CrossRef]
4. Zhang, F. General Introduction to Upconversion Luminescence Materials. In *Photon Upconversion Nanomaterials*; Springer: Berlin/Heidelberg, Germany, 2015. [CrossRef]
5. Tian, Y.; Huang, P.; Wang, L.; Shi, Q.; Cui, C. Efect of Yb^{3+} concentration on upconversion luminescence and temperature sensing behavior in Yb^{3+}/Er^{3+} codoped $YNbO_4$ nanoparticles prepared via molten salt route. *Chem. Eng. J.* **2016**, *297*, 26–34. [CrossRef]
6. Wang, X.; Li, X.; Zhong, H.; Xu, S.; Cheng, L.; Sun, J.; Zhang, J.; Li, L.; Chen, B. Up-conversion luminescence, temperature sensing properties and laser-induced heating effect of Er^{3+}/Yb^{3+}co-doped $YNbO_4$ phosphors under 1550 nm excitation. *Sci. Rep.* **2018**, *8*, 5736. [CrossRef] [PubMed]
7. Ofelt, G.S. Intensities of Crystal Spectra of Rare-Earth Ions. *J. Chem. Phys.* **1962**, *37*, 511–520. [CrossRef]
8. Singh, S.; Kachhap, S.; Sharmaa, M.; Singh, S.K. Enhancing the temperature sensing property of a $Ca_{0.79-x}Bi_xEr_{0.01}Yb_{0.2}MoO_4$ phosphor via local symmetry distortion and reduction in non-radiative channels. *RSC Adv.* **2023**, *13*, 14991–15000. [CrossRef]
9. Thakur, H.; Singh, S.; Gathania, A.K.; Singh, S.K.; Singh, R.K. Effect of $Li^+/K^+/Zn^{2+}$ doping on the optical and temperature sensing properties of Tm^{3+} and Yb^{3+} doped YVO_4 phosphor. *Ceram. Intern.* **2023**, *49*, 25935–25944. [CrossRef]
10. Haase, M.; Schafer, H. Upconverting nanoparticles. *Angew. Chem. Int. Ed.* **2011**, *50*, 5808–5829. [CrossRef]
11. Wang, R.; Zhang, F. NIR luminescent nanomaterials for biomedical imaging. *J. Mater. Chem. B* **2014**, *2*, 2422–2443. [CrossRef]
12. Wei, D.; Qi, J.; Hamblin, M.R.; Wen, X.; Jiang, X.; Yang, H. Near-infrared photoimmunotherapy: Design and potential applications for cancer treatment and beyond. *Theranostics* **2022**, *12*, 7108–7131. [CrossRef]
13. O'Neill, J. *Tackling Drug-Resistant Infection Globally: Final Report and Reccommendations*; Review on Antimicrobial Resistance; Wellcome Trust: London, UK, 2016; p. 80.
14. Alves, E.; Faustino, M.A.F.; Neves, M.G.P.M.S.; Cunha, A.; Tome, J.P.C.; Almeida, A. An insight on bacterial cellular targets of photodynamic inactivation. *Future Med. Chem.* **2014**, *6*, 141–164. [CrossRef]

15. Almeida, A.; Faustino, M.A.F.; Tome, J.P.C. Photodynamic inactivation of bacteria: Finding the effective targets. *Future Med. Chem.* **2015**, *7*, 1221–1224. [CrossRef]
16. Bonnett, R. Photosensitizers of the Porphyrin and Phthalocyanine Series for Photodynamic Therapy. *Chem. Soc. Rev.* **1995**, *24*, 19–33. [CrossRef]
17. Liu, J.J.; Zhang, L.C.; Du, X.J.; Cui, F.X.; Du, C.L.; Gao, B.X. PEG Encapsulation of Porphyrins for Cell Imaging and Photodynamic Therapy. *Lett. Org. Chem.* **2013**, *10*, 342–347. [CrossRef]
18. Zhang, J.L.; Deng, L.; Yao, J.Z.; Gu, P.; Yang, F.; Wang, X.X.; Liu, W.; Zhang, Y.Y.; Ke, X.F.; Jing, X.L.; et al. Synthesis and photobiological study of a novel chlorin photosensitizer BCPD-18MA for photodynamic therapy. *Bioorg. Med. Chem.* **2011**, *19*, 5520–5528. [CrossRef] [PubMed]
19. Noemie, T. Tissue distribution and pharmacokinetics of an ATWLPPR-conjugated chlorin-type photosensitizer targeting neuropilin-1 in glioma-bearing nude mice. *Photochem. Photobiol. Sci.* **2008**, *7*, 433–441. [CrossRef]
20. Isakau, H.A. Toward understanding the high PDT efficacy of chlorin e6-polyvinylpyrrolidone formulations: Photophysical and molecular aspects of photosensitizer-polymer interaction in vitro. *J. Photochem. Photobiol. B* **2008**, *92*, 165–174. [CrossRef]
21. Asano, R.; Nagami, A.; Fukumoto, Y.; Yazama, F.; Ito, H.; Sakata, I.; Tai, A. Synthesis and biological evaluation of new chlorin derivatives as potential photosensitizers for photodynamic therapy. *Bioorg. Med. Chem.* **2013**, *21*, 2298–2304. [CrossRef]
22. Maslenikov, I.I.; Reshetov, V.N.; Useinov, A.S. Mapping the elastic modulus of a surface with a NanoScan 3D scanning microscope. *Instrum. Exp. Tech.* **2015**, *58*, 711. [CrossRef]
23. Malygin, G.A. Plasticity and strength of micro- and nanocrystalline materials. *Phys. Sol. State.* **2007**, *49*, 1013–1033. [CrossRef]
24. Anstis, G.R.; Chantikul, P.; Lawn, B.R.; Marshall, D.B. A Critical Evaluation of Indentation Techniques for Measuring Fracture Toughness: I, Direct Crack Measurements. *J. Am. Ceram. Soc.* **1981**, *64*, 533–538. [CrossRef]
25. Chantikul, P.; Anstis, G.R.; Lawn, B.R.; Marshall, D.B. A Critical Evaluation of Indentation Techniques for Measuring Fracture Toughness: II, Strength Method. *J. Am. Ceram. Soc.* **1981**, *64*, 539–544. [CrossRef]
26. Shannon, R.D. Revised effective ionic radii and systematic studies of interatomic distances in halides and chalcogenides. *Acta Cryst.* **1976**, *32*, 751–767. [CrossRef]
27. Trunov, V.K.; Kinzhibalo, L.N.; Efremov, V.A.; Krongauz, V.G. On the M′-structure of "orthotantalates" of the rare-earth elements. *Dokl. Akad. Nauk SSSR* **1981**, *260*, 103–106.
28. Sanderson, R.T. Chemical Bonds and Bond Energy. Academic Press: New York, NY, USA, 1975.
29. Voloshyna, O.V.; Boiaryntseva, I.A.; Baumer, V.N.; Ivanov, A.I.; Korjik, M.V.; Sidletskiy, O.T. New, dense, and fast scintillators based on rare-earth tantaloniobates. *Nucl. Instrum. Meth. A* **2014**, *764*, 227e231. [CrossRef]
30. Xiao, W.; Yang, Y.; Pi, Z.; Zhang, F. Phase Stability and Mechanical Properties of the Monoclinic, Monoclinic-Prime and Tetragonal $REMO_4$ (M = Ta, Nb) from First-Principles Calculations. *Coatings* **2022**, *12*, 73. [CrossRef]
31. Wu, F.; Wu, P.; Zhou, Y.; Chong, X.; Feng, J. The thermo-mechanical properties and ferroelastic phase transition of $RENbO_4$ (RE = Y, La, Nd, Sm, Gd, Dy, Yb) ceramics. *J. Am. Ceram. Soc.* **2020**, *103*, 2727–2740. [CrossRef]
32. Zhu, J.; Xu, J.; Zhang, P.; Meng, X.; Cao, S.; Wu, J.; Wei, M.; Shi, Y.; Reece, M.J.; Gao, F. Enhanced mechanical and thermal properties of ferroelastic high-entropy rare-earth-niobates. *Scr. Mater.* **2021**, *200*, 113912. [CrossRef]
33. Chen, L.; Hu, M.; Guo, J.; Chong, X.; Feng, J. Mechanical and thermal properties of $RETaO_4$ (RE = Yb, Lu, Sc) ceramics with monoclinic-prime phase. *J. Mater. Sci. Technol.* **2020**, *52*, 20–28. [CrossRef]
34. Suzuki, K.; Kotani, T.; Sato, K. First-principles method justifying the Dieke diagram and beyond. *Phys. Rev. Res.* **2023**, *5*, 013111. [CrossRef]
35. Zhang, D.L.; Hou, Z.P.; Han, F.; Hua, P.R.; Yu, D.Y.; Pun, E.Y.B. Er^{3+} upconversion fluorescence of $ErNbO_4$ phosphor for optical temperature sensing. *IEEE Photon. Technol. Lett.* **2014**, *26*, 1601–1604. [CrossRef]
36. Zhang, D.L.; Hua, P.R.; Cui, Y.M.; Chen, C.H.; Pun, E.Y.B. Absorption and emission characteristics of Er_3NbO_7 phosphor: A comparison with $ErNbO_4$ phosphor and Er:$LiNbO_3$ single crystal. *J. Lumin.* **2007**, *127*, 453–460. [CrossRef]
37. Wang, X.; Li, X.; Cheng, L.; Xu, S.; Sun, J.; Zhang, J.; Zhang, X.; Yang, X.; Chen, B. Concentration-dependent spectroscopic properties and temperature sensing of $YNbO_4$:Er^{3+} phosphors. *RSC Adv.* **2017**, *7*, 23751–23758. [CrossRef]
38. Singh, S.; Kachhap, S.; Singh, A.K.; Pattnaik, S.; Singh, S.K. Temperature sensing using bulk and nanoparticles of $Ca_{0.79}Er_{0.01}Yb_{0.2}MoO_4$. *Methods Appl. Fluoresc.* **2022**, *10*, 044004. [CrossRef]
39. Hirano, M.; Ishikawa, K. Hydrothermal formation and up-conversion luminescence of Er^{3+}-doped $GdNbO_4$. *J. Am. Ceram. Soc.* **2017**, *100*, 2814–2821. [CrossRef]
40. Blasse, G.; Bril, A. Luminescence phenomena in compounds with fergusonite structure. *J. Lumin.* **1970**, *3*, 109–131. [CrossRef]
41. Blasse, G.; Bril, A. Photoluminescent Efficiency of Phosphors with Electronic Transitions in Localized Centers. *J. Electrochem. Soc.* **1968**, *115*, 1067–1076. [CrossRef]
42. Palatnikov, N.; Smirnov, M.V.; Masloboeva, S.M.; Shcherbina, O.B.; Sidorov, N.V.; Steblevskay, N.I.; Belobeletskaya, M.V. Luminescence properties of Sol–Gel Derived Ceramic $GdNb_xTa_{1-x}O_4$ and $YNb_xTa_{1-x}O_4$ Solid Solutions. *Inorg. Mat.* **2020**, *56*, 437–442. [CrossRef]

43. Nitzan, Y.; Gutterman, M.; Malik, Z.; Ehrenberg, B. Inactivation of gram-negative bacteria by photosensitized Porphyrins. *Photochem. Photobiol.* **1992**, *55*, 89–96. [CrossRef]
44. Raetz, C.R.; Ulevitch, R.J.; Wright, S.D.; Sibley, C.H.; Ding, A.; Nathan, C.F. Gram-negative endotoxin an extraordinary lipid with profound effects on eukaryotic transduction. *FASEB J.* **1991**, *5*, 2652–2660. [CrossRef]
45. Hamblin, M.R.; Gasan, T. Photodynamic therapy: A new antimicrobical approach to infectious desease. *Photochem. Photobiol. Sci.* **2004**, *3*, 436–450. [CrossRef] [PubMed]
46. Ergaieg, K.; Chevanne, M.; Cillard, J.; Seux, R. Involvement of both Type I and Type II mechanisms in Gram-positive and Gram-negative bacteria photosensitization by a meso-substituted cationic porphyrin. *J. Sol. Energy* **2008**, *82*, 1107–1117. [CrossRef]

Disclaimer/Publisher's Note: The statements, opinions and data contained in all publications are solely those of the individual author(s) and contributor(s) and not of MDPI and/or the editor(s). MDPI and/or the editor(s) disclaim responsibility for any injury to people or property resulting from any ideas, methods, instructions or products referred to in the content.